Using the dynamic, expanding liquid–liquid interface in a Hele–Shaw cell in crystal growth and nanoparticle assembly

Debabrata Rautaray, Ritwik Kavathekar and Murali Sastry*

Materials Chemistry Division, National Chemical Laboratory, Pune 411008, India. E-mail: sastry@ems.ncl.res.in; Fax: +91 20 25893952/25893044; Tel: +91 20 25893044

Received 14th April 2004, Accepted 7th May 2004
First published as an Advance Article on the web 16th September 2004

The liquid–liquid interface has been used with considerable success in the synthesis of advanced materials ranging from (bio)minerals to inorganic membranes to nanoparticles. In almost all such cases, the interface is static. The Hele–Shaw cell in which a viscous fluid is displaced by a less viscous one in a constrained manner has been invaluable in the study of dynamic instabilities at interfaces and in the study of viscous fingering pattern formation. However, the potential of the Hele–Shaw cell in carrying out reactions at the interface between the two fluids leading to the formation of inorganic materials has been largely unrecognized and underexploited. Realizing that the dynamic liquid–liquid interface in a Hele–Shaw cell would provide opportunities to control a variety of time-scales associated with material formation, we have started a program on the use of the Hele–Shaw cell in materials synthesis. In this discussion paper, we present some of our recent results on the growth of calcium carbonate crystals in the Hele–Shaw cell by the reaction of Ca^{2+} ions electrostatically complexed with carboxylate ions pinned to the interface with carbonate ions present in the aqueous part of the biphasic reaction medium. We show that both polymorph selectivity and the morphology of the crystals may be modulated by varying the experimental conditions in the cell. We also discuss the possibility of using the dynamic interface in the Hele–Shaw cell to cross-link gold nanoparticles in water through bifunctional linkers present in the oil phase and investigate the nature of the structures formed.

Introduction

Synthesis of advanced inorganic materials with control over structure, size and morphology is often driven by commercial requirements in areas as diverse as electronics, pigments and cosmetics, ceramics and medical industries.[1,2] Insofar as materials engineering is concerned, much of the research has centered on the use of biomimetic templates such as Langmuir monolayers at the air–water[3–9] and liquid–liquid interface,[10,11] self-assembled monolayers (SAMs),[12–15] lipid bilayer stacks[16–18] and functionalized polymer surfaces[19–21] to achieve such control.

Liquid–liquid interfaces play a critical role in many chemical, physical, and biological processes. The past decade has witnessed a huge increase of research interest in the study of liquid–liquid interfaces, fueled in part by new experimental and theoretical methods. Interfaces play a key role in modern science and technology and the unique features and phenomena induced in them have attracted the interest of researchers in many different fields. In particular, liquid–liquid interfaces

have drawn much attention; not only do these interfaces have structural and dynamical nonlinear properties which are not observed in bulk liquids, but also they are integral to many chemical and biological systems.[22]

The liquid–liquid interface is important in various chemical processes such as phase transfer catalysis,[23–29] solvent extraction,[26] and ion-selective electrode operation.[25,30] Phase transfer catalysis at the liquid–liquid interface has attracted much attention because reaction rates are considerably enhanced by transfer across the liquid–liquid interface to yield high product and selectivity,[31–33] separation and recovery[29] and reuse of the catalyst[23] while maintaining high levels of catalytic activity. The liquid–liquid interface also offers a fertile medium for the assembly of nanoparticles,[34–40] and for the chemical manipulation of nanoparticles.[36] For example, interfaces between immiscible fluids, *i.e.*, on the surface of droplets, have been shown to be ideal for the assembly of elastic, semipermeable capsules composed of micrometer-sized colloidal particles.[41,42] Self-assembly of chemically functionalized nanoparticles at the toluene–water interface, coupled with chemical crosslinking of the attached ligands, provides a simple and flexible route for the fabrication of ultrathin, composite organic–inorganic membranes.[42] Efrima and co-workers first demonstrated that metal liquid-like films (MELLFs) of silver could, under stringent conditions, be synthesized at the interface between an organic solvent such as dichloromethane and water.[37,38] Subsequent reports have developed on this approach and the organization of negatively charged colloidal gold particles *via* electrostatic interactions with cationic surfactant molecules,[39] and the assembly of gold nanoparticles into one-dimensional superstructures[40] at the liquid–liquid interface have been shown. The controlled assembly of nanoparticles both in solution and on suitable surfaces is a problem of current interest with direct relevance to commercial applications of nanoscale matter. Interparticle interactions have also been studied at liquid–liquid interfaces.[36,43] For example oxides such as TiO_2 and metals such as Au nanoparticles can be assembled at the interface upon applying a potential bias[44,45] between two immiscible electrolyte solutions.[46] The transferring of monolayers from liquid–liquid interfaces using the Langmuir–Blodgett technique has also been studied in great detail.[47–49]

The liquid–liquid interface is of considerable importance in biological systems, particularly in biomedical engineering, pharmacology, and food processing. For example, the hydrocarbon–water interface provides an excellent medium to cellular interfaces where many important biological functions and/or processes occur.[50] These include receptor–ligand interactions, energy transduction, electron transfer, enzyme coupling, and triggering of cells by hormones and neurotransmitters.[50] The liquid–liquid interface provides an excellent model for interactions of macromolecules at relatively mobile interfaces as well.[50] The liquid–liquid interface is also crucial to food systems and food processing. For example, the distribution and/or interactions of proteins and surfactants at this interface greatly influences the properties of food emulsions and microemulsions.[51]

The important biomineral calcium carbonate has been studied in much detail due to its abundance in nature and also its vast industrial application. Calcium carbonate is a relatively complex mineral system due to the existence of three stable polymorphs calcite, aragonite and vaterite.[52] Calcium carbonate crystallization has been achieved under Langmuir monolayers,[53] within lipid bilayer stacks,[17] using polymers,[19] bicontinuous emulsions,[54] using mixed solutions of surfactants and block copolymers,[55] on functionalized gold nanoparticles,[56] monolayer films of gold nanoparticles,[57] as well as on free nanoparticles in solution.[58] The synthesis of gold nanoparticles has also received considerable attention due to their interesting applications in single electron tunneling[59] and non-linear optical devices.[60] There is a growing interest in the organization of nanoparticles in two- and three-dimensional structures. The main challenge in this area is to develop protocols for the organization of crystalline arrays of nanoparticles wherein both the size and separation between the nanoparticles in the arrays can be tailored. Applications based on the collective properties of the organized particles require flexibility in controlling the nanoarchitecture of the film.[61] Attempts have been made to assemble nanoparticles in two-dimensional structures by a variety of methods that include self-assembly of the particles during solvent evaporation,[62] immobilization by covalent attachment at the surface of the self-assembled monolayers,[14,15] or surface modified polymers,[63] electrophoretic assembly onto suitable substrates,[64] electrostatic attachment to Langmuir monolayers at the air–water interface[7–9] and air–organic solvent interface,[11] and by diffusion into ionizable fatty lipid films.[18] Attempts have also been made to synthesize oxides such as zinc oxide,[65] gallium oxide,[66] and ceramics such as $BaCrO_4$[67] and $BaSO_4$[68–70]

particularly in microemulsions where interactions between surfactant molecules coating the crystallites were implicated in the assembly process.[67,68–70]

From the above discussions, it is clear that the liquid–liquid interface has been extensively investigated in the synthesis of advanced materials. However, in all these studies, the interface (often charged due to the presence of ionizable surfactants) was *static* and other than providing a scaffold on which material growth could take place, was more or less passive. The idea of generating *expanding* liquid–liquid interfaces and investigating their role in modulating the morphology/crystallography of inorganic materials grown at these interfaces is a relatively new one developed in this laboratory and in terms of understanding, is still at an elementary stage. In order to achieve controllable expanding liquid–liquid interfaces for growth of materials, we have used a Hele–Shaw cell[71] commonly used by physicists to study the phenomenon of viscous fingering.[71] The schematic of the process is given in Fig. 1A and consists of injecting a less viscous immiscible liquid into another that is constrained between two parallel plates. In our first set of experiments, we have studied the growth of the minerals $BaSO_4$[72] and $CaCO_3$[73] in a radial Hele–Shaw cell (Fig. 1A) as model systems. This was accomplished by taking the fatty acids such as stearic acid/aerosol OT in the organic phase and carrying out the reaction of the appropriate metal ions (Ba^{2+}/Ca^{2+}) with the corresponding counterions (SO_4^{2-}/CO_3^{2-}) present in the aqueous phase (injected phase). The reaction leading to mineral formation occurred at the interface due to strong complexation of the metal cations with the charged fatty acid/AOT leading to unusual morphologies of the crystals.[72,73] In the case of $BaSO_4$ crystals, it was observed that the crystals were organized into highly linear superstructures over large length-scales[72] whereas in the case of $CaCO_3$ crystallization, we have observed the room temperature growth of almost phase-pure aragonite needles.[73] By judicious choice of the experimental parameters in the Hele–Shaw cell, we have achieved control over the degree of recrystallization of aragonite to calcite and thus, have obtained crystals with hollow, cylindrical morphology.[73]

In this Faraday discussion paper, we address the issue of expanding liquid–liquid interfaces in materials synthesis in greater depth and present results of our investigation of two problems. The first concerns the role of viscosity in determining the morphology and assembly of $CaCO_3$ crystals

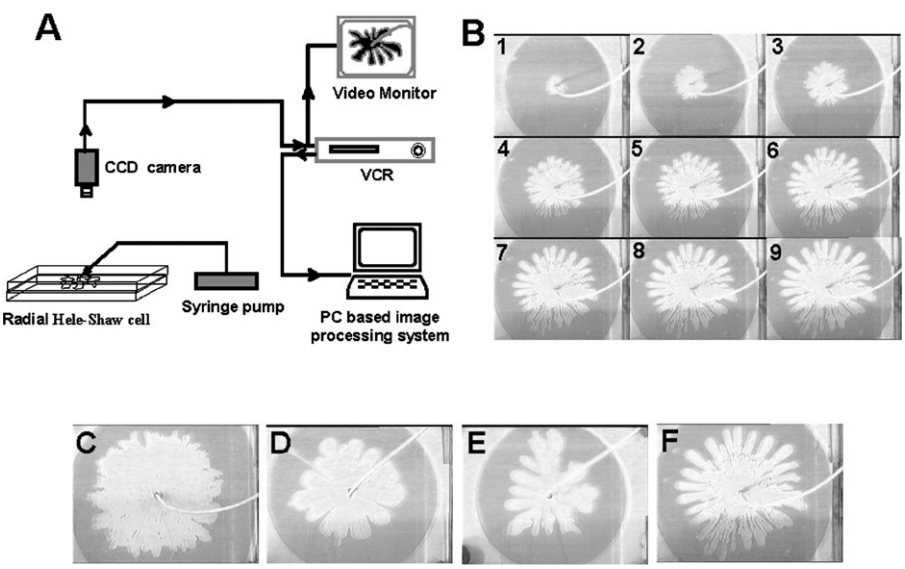

Fig. 1 (A) Schematic showing the various elements in the radial Hele–Shaw experiment. (B) Images of the patterns recorded at different times during injection of aqueous solution of $CaCl_2$ and Na_2CO_3 (transparent phase) into the AOT–chloroform–paraffin solution (colored phase). (C–F) Images of the patterns formed at the end of injection of aqueous solutions of $CaCl_2$ and Na_2CO_3 (transparent phase) into the AOT–chloroform–paraffin phase of different viscosities: C, 0.002678 Pa s; D, 0.003434 Pa s; E, 0.00488 Pa s and F, 0.046 Pa s (see text for details).

grown in a radial Hele–Shaw cell. We have also studied, for the first time, the assembly of gold nanoparticles using bifunctional linker molecules at an expanding liquid–liquid interface. Presented below are the details of this study.

Experimental

The radial Hele–Shaw cell used in this study was composed of two 1 cm thick, 30×30 cm^2 float-glass plates. Spacers of thickness $b = 300$ μm were used between the top and bottom glass plates. The viscous fluid [mixture of a solution of chloroform containing AOT ($C_{20}H_{37}NaO_7S$, MW = 444.56, 1×10^{-3} M) and paraffin] was taken in the cell gap and thereafter, an aqueous solution containing $CaCl_2$ and Na_2CO_3 at salt solution supersaturation (S_R) of 30 (10 mL of 1×10^{-2} M aqueous $CaCl_2$ and 10 mL of 1.36×10^{-3} M aqueous Na_2CO_3) was injected through a hole (0.5 mm diameter) drilled at the center of the top glass plate, using an automated fluid delivery system (Fig. 1A). Experiments were performed at five different solution viscosities by varying the AOT–chloroform solution : paraffin ratios of 4 : 1 (viscosity, $\eta = 0.002678$ Pa s), 1.5 : 1 ($\eta = 0.003434$ Pa s), 1 : 1 ($\eta = 0.00412$ Pa s), 1 : 1.5 ($\eta = 0.00488$ Pa s) and 1 : 4 ($\eta = 0.046$ Pa s) as the displaced fluid at a constant plate separation (S_P) of 300 μm. A small amount of dye was added to the chloroform–paraffin mixture to yield sufficient contrast between the aqueous and organic solutions for easy capture of the images with a CCD (charge-coupled device) camera (Fig. 1A). The experiments were performed at a constant volumetric flow rate (VFR) of 0.5 ml min^{-1}. The evolution of the finger pattern with time was followed for the above cases using a CCD camera connected to a video recorder at an image capture rate of 25 images s^{-1} (Fig. 1A). On completion of the injection process (typically 15–20 min), the organic solution was carefully removed and the remaining aqueous $CaCO_3$ precipitate was washed with copious amounts of doubly distilled water and placed on Si(111) wafers and on glass substrates for scanning electron microscopy (SEM)/energy dispersive analysis of X-rays (EDAX), Fourier transform infrared spectroscopy (FTIR) and X-ray diffraction (XRD) measurements, respectively.

Samples for SEM and EDAX measurements were prepared by drop-coating films of the $CaCO_3$ crystals on Si(111) wafers. These measurements were carried out on a Leica Stereoscan-440 scanning electron microscope equipped with a Phoenix EDAX attachment. EDAX spectra were recorded in the spot-profile mode by focusing the electron beam onto specific regions of the film. Fourier transform infrared spectroscopy (FTIR) measurements were carried out in the diffuse reflectance mode at a resolution of 2 cm^{-1} on a Perkin–Elmer FTIR-Spectrum One instrument. XRD analysis of the $CaCO_3$ drop-coated films on glass substrates were carried out on a Phillips PW 1830 instrument operating at a voltage of 40 kV and a current of 30 mA with Cu Kα radiation.

The Hele–Shaw set up was also used for assembling gold nanoparticles at the expanding liquid–liquid interface. In this experiment, a viscous fluid [mixture of toluene containing ethylenediamine (NH_2–CH_2–CH_2–NH_2) and paraffin] was taken in the cell gap and thereafter, an aqueous solution of sodium borohydride reduced gold nanoparticles was injected into the Hele–Shaw cell. This experiment was performed with a viscous solution of toluene and paraffin in the ratio of 1 : 4 (viscosity, $\eta = 0.043$ Pa s) as the displaced fluid with a constant plate separation of 300 μm and a steady VFR of 0.5 ml min^{-1}. In another experiment, the assembly of gold nanoparticles was carried out using the radial Hele–Shaw cell where an aqueous solution of sodium borohydride reduced aqueous gold nanoparticles was taken in the cell gap and thereafter, chloroform containing ethylenediamine was injected into the cell at a constant S_P of 300 μm and a constant VFR of 0.5 ml min^{-1}. On completion of the injection process, the organic solutions were carefully removed in both experiments and the remaining aqueous solutions were characterized by UV-visible spectroscopy (UV-vis) and transmission electron microscopy (TEM) measurements.

UV-vis spectroscopy measurements were carried out on a Jasco-V-570 UV/VIS/NIR spectrophotometer operated at a resolution of 2 nm. Samples for TEM analysis were prepared by drop-coating films of the Au nanoparticle solutions onto carbon-coated copper TEM grids, allowing the grids to stand for 2 min following which the extra solution was removed using a blotting paper. TEM analysis of the gold nanoparticle samples was carried out on a JEOL model 1200EX instrument operated at an accelerating voltage of 120 kV.

Results and discussion

The displacement of a viscous fluid by a less viscous one leads to the formation of finger-like patterns known as 'viscous fingering'.[71] The morphology of the viscous-finger patterns generated is a function of many parameters such as the flow rate, difference in viscosities of the two fluids and the interfacial tension. In the first part of this study, we investigate the role of variation in viscosity of the displaced phase in modulating the morphology of $CaCO_3$ crystals grown at the liquid–liquid interface. This represents an important advance on our preliminary investigation into $CaCO_3$ growth in a Hele–Shaw cell presented earlier.[73] We recollect that the $CaCO_3$ crystals are grown by reaction of an injected aqueous solution of $CaCO_3$ into a viscous chloroform–paraffin mixture containing the surfactant AOT (scheme in Fig. 1A). Fig. 1B shows pictures of the Hele–Shaw cell showing the evolution of the finger patterns with time recorded during the injection of an aqueous solution of $CaCl_2$ and Na_2CO_3 into the AOT–chloroform–paraffin mixture ($\eta = 0.046$ Pa s). As can be seen in Fig. 1B, the viscous fingering pattern evolves as the injection of the aqueous phase into the organic phase proceeds (time of injection increasing from 1–9). At completion of the injection, the highly branched, viscous fingering pattern is clearly seen. The viscous fingering patterns obtained in separate experiments where the viscosity of the organic phase was varied is shown in Fig. 1C–F [$\eta = 0.002678$ Pa s (C); 0.003434 Pa s (D); 0.00488 Pa s (E) and 0.046 Pa s (F)]. One can clearly notice the significant variation in the morphologies of the branched patterns for the different viscosities of the displaced fluid used. As the viscosity increases, the morphology of the patterns become progressively more branched (Fig. 1C–F). The fractal dimensions of the patterns have been determined for the different viscosities used and are listed in Table 1. It is observed that there is an increase in the fractal dimensions (Table 1) on increasing the viscosity of the displaced organic phase supporting the increase in the complexity of the patterns observed (Fig. 1C–F).

It should be pointed out that the flow rate was decided based upon the induction time observed for initiation of crystal nucleation. The slow VFR coupled with the difference in viscosities of the two fluids[74] is responsible for the complex, branched interface and thus provides a model system for understanding crystal growth processes at such dynamic liquid–liquid interfaces.

Fig. 2A and B show representative SEM images at different magnifications of the $CaCO_3$ crystals grown in the Hele–Shaw cell during displacement of the AOT–chloroform–paraffin organic phase ($\eta = 0.002678$ Pa s) by an aqueous solution of $CaCl_2$ and Na_2CO_3 at an S_R of 30. The substrate was densely populated with flower-like $CaCO_3$ crystals (Fig. 2A). The inset of Fig. 2A shows a magnified view of a few of the crystallites in greater detail showing that most of the flower-like $CaCO_3$ crystals consist of either four or six petals and that the petals originate from a central point. Fig. 1B shows the flower-like $CaCO_3$ crystals consisting of six petals in finer detail. The petals of the $CaCO_3$ crystals appear to be extremely thin and flat. The inset of Fig. 2B clearly shows the flatness of the $CaCO_3$ crystals. The length of the $CaCO_3$ petals in the flower-like assemblies is in the range of 300–600 nm while the widths are typically in the range of 200–300 nm. From the SEM images, we are unable to estimate the thickness of the $CaCO_3$ petals. EDAX analysis of the petals in the $CaCO_3$ flowers (curve 1, Fig. 3A) yielded a Ca : C : O atomic ratio close to the expected stoichiometry. Along with expected Ca, C and O, strong signals of Na and S components from the surfactant AOT are seen indicating surface binding of the AOT molecules to the $CaCO_3$ petals. The FTIR spectrum

Table 1 Details of the fractal dimensions of the finger patterns, viscosity of the organic phase and observed morphology of $CaCO_3$ crystals in the Hele–Shaw cell experiments

Obs No.	Mixture of chloroform : paraffin	Viscosity/ Pa s	Fractal dimension (FD)	Morphology of $CaCO_3$ crystals formed
1	4 : 1	0.002678	1.88 (± 0.03)	Flower like calcite with two/four petals
2	1.5 : 1	0.003434	1.91 (± 0.01)	Flower like calcite as well as patterned structures
3	1 : 1	0.00412	1.94 (± 0.01)	Patterned calcite with regular steps
4	1 : 1.15	0.00488	1.97 (± 0.02)	Patterned calcite with smaller and sharper crystallites
5	1 : 4	0.046	1.99 (± 0.01)	Patterned calcite assemblies

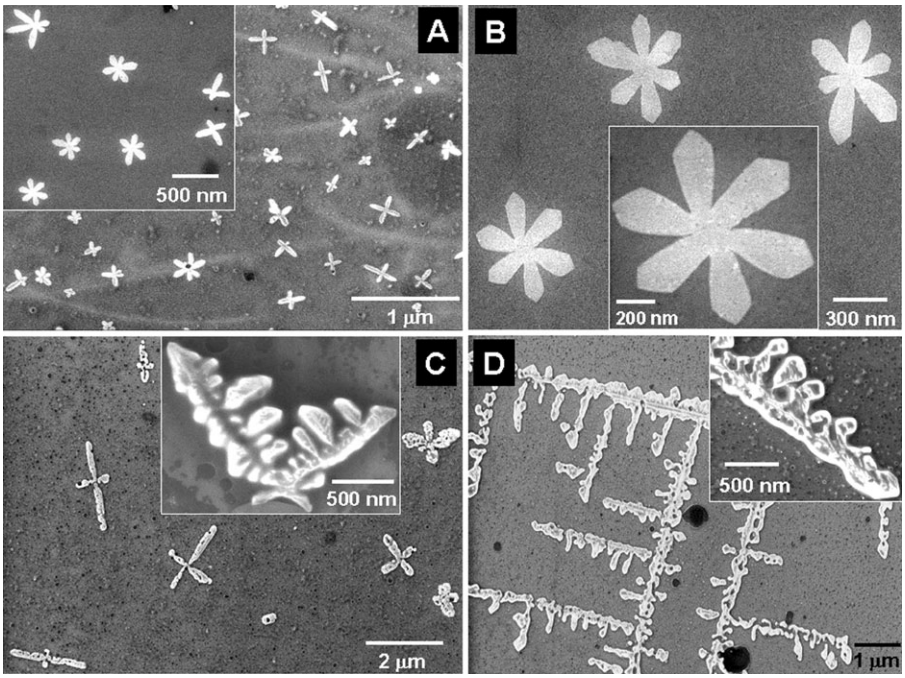

Fig. 2 (A and B)—Low and high magnification SEM images, respectively, of $CaCO_3$ crystals grown in the Hele–Shaw cell with an organic phase viscosity of 0.002678 Pa s. (C and D)—Low and high magnification SEM images, respectively, of $CaCO_3$ crystals grown in the Hele–Shaw cell with an organic phase viscosity of 0.003434 Pa s. The insets in all the figures show magnified views of representative $CaCO_3$ crystals in the main part of the figure (see text for details).

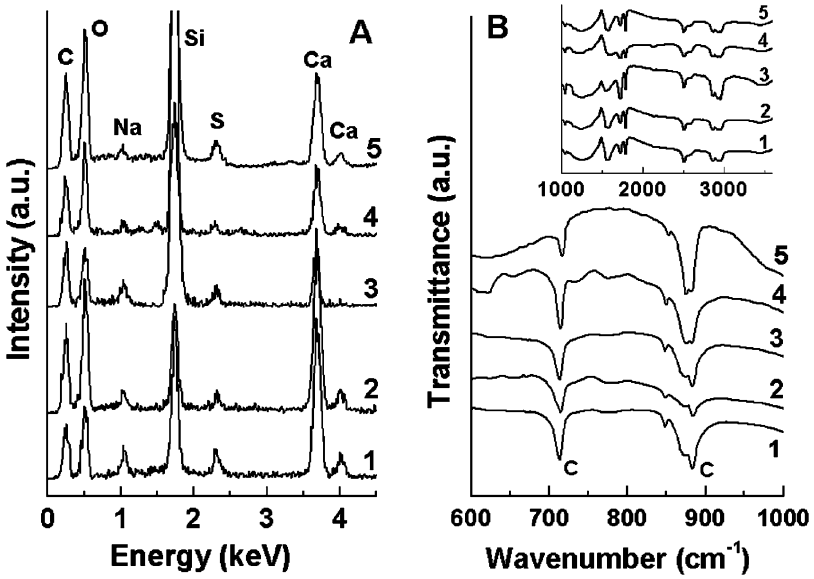

Fig. 3 (A) Spot-profile EDAX spectra recorded from the films of $CaCO_3$ crystals grown in the Hele–Shaw cell with organic phase viscosities of 0.002678 Pa s (curve 1); 0.003434 Pa s (curve 2); 0.00412 Pa s (curve 3); 0.00488 Pa s (curve 4) and 0.046 Pa s (curve 5). (B and inset) FTIR spectra in different spectral windows recorded from: $CaCO_3$ crystals grown in the Hele–Shaw cell with organic phase viscosities of 0.002678 Pa s (curve 1); 0.003434 Pa s (curve 2); 0.00412 Pa s (curve 3); 0.00488 Pa s (curve 4) and 0.046 Pa s (curve 5).

recorded from the $CaCO_3$ flowers is shown as curve 1 in Fig. 3B. The absorption bands at 712 and 872 cm^{-1} are characteristic of calcite.[75] Prominent absorption bands are also seen at 1056, 1700, 2850 and 2950 cm^{-1} (curve 1 in the inset of Fig. 3B). The band at 1056 cm^{-1} is assigned to the S=O stretching vibration of the sulfonate group present in the surface-bound AOT molecules.[76] The band at 1700 cm^{-1} is due to carbonyl stretch vibrations in the AOT molecules and the two bands at 2850 and 2950 cm^{-1} have been assigned to the methylene symmetric and antisymmetric stretching vibrations in the hydrocarbon chains, respectively. The XRD pattern recorded from the flower-like $CaCO_3$ crystals shown in Fig. 1A and B is displayed as curve 1 in Fig. 4. It is observed that the $CaCO_3$ crystals formed in this experiment consist of predominantly the calcite polymorph.[77]

Fig. 2C and D show SEM images at different magnifications of $CaCO_3$ crystals grown in the Hele–Shaw cell during the displacement of AOT–chloroform–paraffin organic solution ($\eta = 0.00412$ Pa s) by an aqueous solution of $CaCl_2$ and Na_2CO_3 at an S_R of 30. In this experiment we observe both $CaCO_3$ crystals with flower-like morphology (Fig. 2C) as well as more extended, quasi-linear superstructures of $CaCO_3$ crystals (Fig. 2D). The $CaCO_3$ flowers shown at the lower magnification (Fig. 2C) appear on a gross scale to be quite similar to those obtained in the lower viscosity experiment (Fig. 2A). At higher magnification, however (inset of Fig. 2C) differences are observed. The petals in the $CaCO_3$ flowers are not smooth and flat as in the earlier experiment. Furthermore, the presence of the highly branched linear structures of the crystals appears to be related to an increase in viscosity of the displaced fluid which, as seen in the images of the patterns formed for different viscosities of the organic phase (Fig. 1C–F), can be correlated with increasing complexity of the viscous-fingering patterns during the injection process. The inset in Fig. 2D shows a high magnification SEM image of a particular region of the quasi-linear $CaCO_3$ crystals clearly revealing the branched nature of the $CaCO_3$ structures. EDAX analysis of the $CaCO_3$ crystals shown in Fig. 2C and D yielded a Ca : C : O atomic ratio close to the expected stoichiometry along with Na and S components from the AOT capping layer (curve 2 in Fig. 3A). The FTIR spectrum (curve 2 in Fig. 3B) and XRD pattern (curve 2 in Fig. 4) recorded from this sample revealed the formation of the polymorph, calcite.

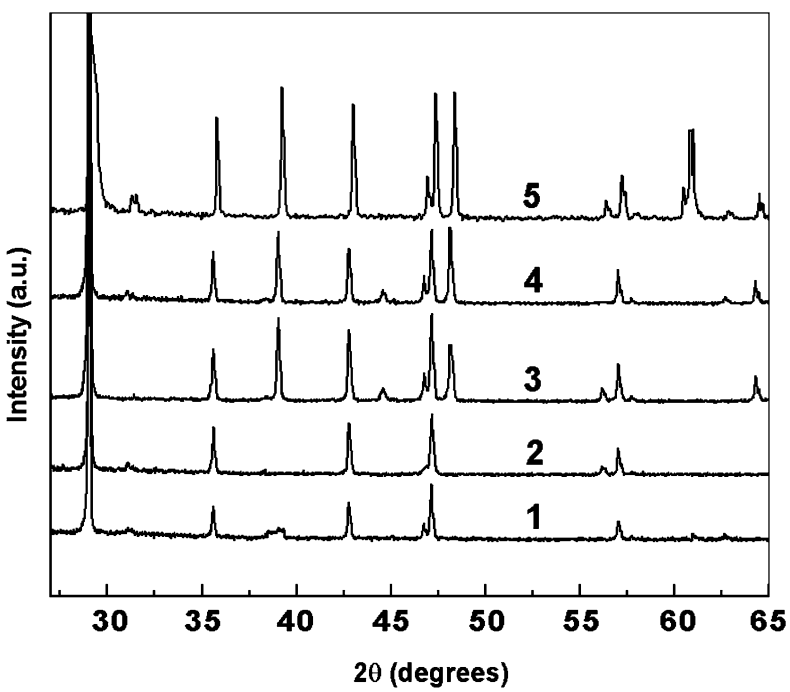

Fig. 4 XRD patterns recorded from $CaCO_3$ crystals synthesized in the radial Hele–Shaw cell with organic phase viscosities of 0.002678 Pa s (curve 1); 0.003434 Pa s (curve 2); 0.00412 Pa s (curve 3); 0.00488 Pa s (curve 4) and 0.046 Pa s (curve 5).

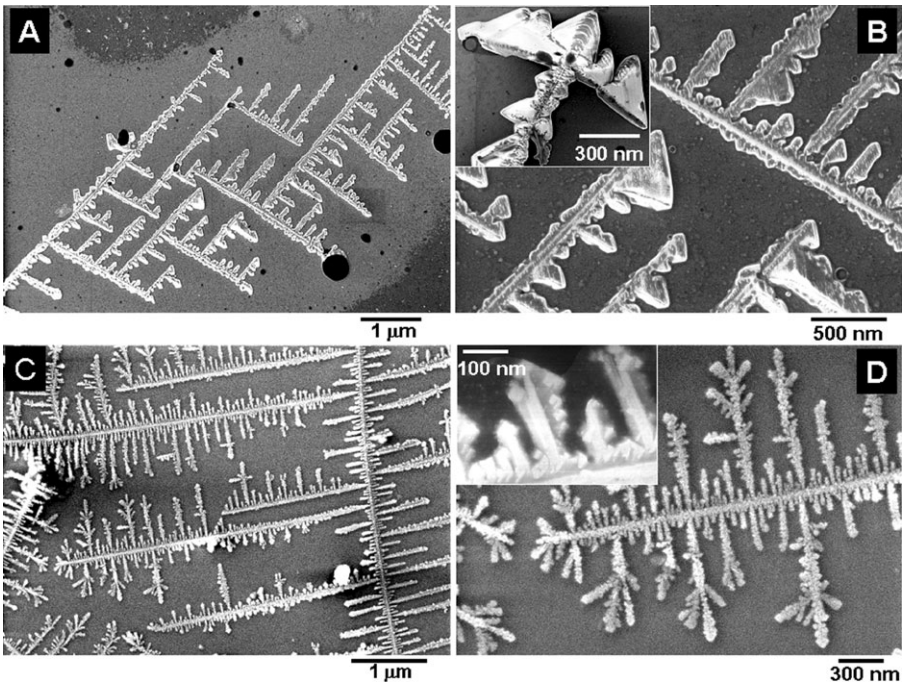

Fig. 5 (A and B)—Low and high magnification SEM images, respectively, of $CaCO_3$ crystals grown in the Hele–Shaw cell with an organic phase viscosity of 0.00412 Pa s. (C and D)—Low and high magnification SEM images, respectively, of $CaCO_3$ crystals grown in the Hele–Shaw cell with an organic phase viscosity of 0.00488 Pa s. The insets in B and D show a magnified view of representative crystals shown in the main part of the figure.

Fig. 5A and B show SEM images at different magnification of $CaCO_3$ crystals grown in the Hele–Shaw cell during the displacement of AOT–chloroform–paraffin ($\eta = 0.003434$ Pa s) by an aqueous solution of $CaCl_2$ and Na_2CO_3 at an S_R of 30. In gross detail, the $CaCO_3$ structures that are formed are similar to those synthesized in the Hele–Shaw cell at an organic solution viscosity of 0.002678 Pa s. The $CaCO_3$ crystals in this experiment exhibit a highly branched morphology, with evidence of secondary nucleation and growth around a linear 'core' (Fig. 5A). The higher magnification SEM image (Fig. 5B) shows that the edges of the $CaCO_3$ crystals are very sharp with steps observed regularly on the $CaCO_3$ super structures (inset of Fig. 5B). Similar steps have been observed previously on calcite crystals.[78,79] Orme *et al.* have observed such steps in calcite crystals where they have found that site-specific binding of amino acid residues to surface steps changes the step-edge free energies, thereby giving rise to modifications that propagate from atomic length scales to macroscopic length scales.[78] Sugawara *et al.* have succeeded in preparing periodically patterned $CaCO_3$ films with regular surface relief structures on a thin matrix of cholesterol-modified pullulan from an aqueous solution containing poly(acrylic acid).[79] That similar structures may be obtained in an experiment involving crystal growth at a dynamic liquid–liquid interface is an interesting outcome of this work.

The EDAX measurements from the patterned $CaCO_3$ structures obtained above (curve 3 in Fig. 3A) indicated the presence of Ca, C and O along with Na and S arising from surface-bound AOT molecules. The formation of the calcite polymorph is confirmed by FTIR (curve 3 in Fig. 3B) and XRD analysis (curve 3 in Fig. 4). Fig. 5C and D show SEM images of $CaCO_3$ crystals grown in the Hele–Shaw cell during the displacement of AOT–chloroform–paraffin ($\eta = 0.00488$ Pa s) by an aqueous solution of $CaCl_2$ and Na_2CO_3 under conditions identical to the other experiments. In keeping with the trend, an increase in viscosity leads to an enhancement of the branched calcite structures, as observed in Fig. 5C. The individual crystallites in the branched assemblies are thinner and finer than those observed in the lower viscosity experiments (Fig. 5D). There also appears to be more secondary crystal growth on both sides of the linear axis. The higher magnification SEM

image (inset of Fig. 5D) clearly shows that the branches are in turn made up of smaller crystallites with sharp edges. EDAX analysis confirms the presence of Ca, C and O in the right stoichiometric ratio along with Na and S from surface-bound AOT molecules (curve 4 in Fig. 3A). The FTIR (curve 4 in Fig. 3B) and XRD (curve 4 in Fig. 4) data confirm that the structures observed are indeed calcite crystals.

At the highest viscosity studied ($\eta = 0.046$ Pa s), the fingers formed in the radial Hele–Shaw cell are at their narrowest (Fig. 1E) and the corresponding fractal dimension is the highest. Fig. 6A–D show SEM images at different magnification of $CaCO_3$ crystals grown in the Hele–Shaw cell involving the experiment in the organic phase being of this viscosity. The increase in complexity of the finger patterns seen in Fig. 1E has clearly translated into the formation of quasi-linear, patterned assemblies of $CaCO_3$ crystals of very large length scales (Fig. 6A and B) densely populating the substrate surface. In some regions, the growth of the calcite crystals is very irregular (Fig. 6C). The higher magnification SEM image of one of the ordered assemblies (Fig. 6D) clearly shows that the $CaCO_3$ crystals are in fact assemblies of smaller $CaCO_3$ crystallites and also that in this case, growth of the secondary crystals proceeds out of the plane of the substrate as well (inset, Fig. 6D). The EDAX spectrum from the $CaCO_3$ crystals assemblies observed in Fig. 6 showed the expected Ca, C and O signals at stoichiometric ratios along with strong signals of Na and S from the AOT surface monolayer (curve 5 in Fig. 3A). FTIR analysis from the $CaCO_3$ crystal assemblies show characteristic strong absorption bands at 712 and 872 cm^{-1} which are attributed to the calcite polymorph (curve 5 in Fig. 3B). The absorption band at 1056 cm^{-1} arises from S=O stretching vibration of the sulfonate group present in the AOT molecules (curve 5 in the inset of Fig. 3B). The XRD pattern recorded from the patterned $CaCO_3$ assemblies shown in Fig. 6 is displayed as curve 5 in Fig. 4 indicating the formation of calcite polymorph in this case as well. One interesting observation in all the XRD spectra (curves 1–5 in Fig. 4) is the gradual appearance of new Bragg peaks as the organic phase viscosity increases.

To demonstrate the generality of this method for not only growing but assembling inorganic materials as well, we have examined the possibility of cross-linking gold nanoparticles using bifunctional molecules such as ethylenediamine at the expanding liquid–liquid interface. The assembly of Au nanoparticles was achieved using the Hele–Shaw cell by injecting an aqueous solution of sodium borohydride reduced gold nanoparticles into a solution of toluene containing diamine and paraffin having a viscosity of 0.046 Pa s. During injection of the nanoparticle solution, it is expected that the diamine molecules present at the interface would complex with gold nanoparticles leading to their aggregation at the interface. It is known that amine groups bind strongly with gold nanoparticles,[80–84] and therefore, this is expected to be a new strategy for nanoparticle assembly. Fig. 7A shows a representative viscous fingering pattern recorded during the injection of borohydride reduced gold nanoparticles (colored phase) into a mixed solution of toluene containing diamine and paraffin (transparent phase) showing the complex fingering pattern formed (Fig. 7A).

Fig. 7B shows the UV-vis spectra recorded from pure paraffin solution (curve 1) and from the sodium borohydride reduced gold nanoparticle solution before injection into the Hele–Shaw cell (curve 2). It is observed that there is no evidence of absorption in the 400–800 nm window region of the electromagnetic spectrum from pure paraffin solution (curve 1). The gold nanoparticles show a prominent and sharp absorption band at 520 nm. This absorption band is characteristic of gold nanoparticles and arises due to excitation of surface plasmon vibrations in the nanoparticles. Curve 3 in Fig. 7B shows the UV-vis spectrum of gold nanoparticles assembled in the Hele–Shaw cell during the injection of an aqueous solution of sodium borohydride reduced gold nanoparticles into the toluene solution of the diamine and paraffin having a viscosity of 0.046 Pa s. Two absorption bands at 526 and 640 nm are observed in the UV-vis spectrum from these gold nanoparticles. The absorption band at 526 nm is due to out-of-plane plasmon vibrations in the particles while the longer wavelength absorption band (640 nm) arises due to excitation of the in-plane plasmon vibration from aggregates of the gold nanoparticles.[85] It is well known that highly dispersed Au nanoparticles in solution exhibit only a single peak at 520 nm while crosslinked particles show two absorption maxima. As the aspect ratio of the aggregates increases, the in-plane plasmon peak intensifies and shifts to longer wavelengths.[85]

Fig. 8A–C show representative TEM images at different magnifications of Au nanoparticle assemblies formed in the Hele–Shaw cell experiment discussed above. As was indirectly inferred

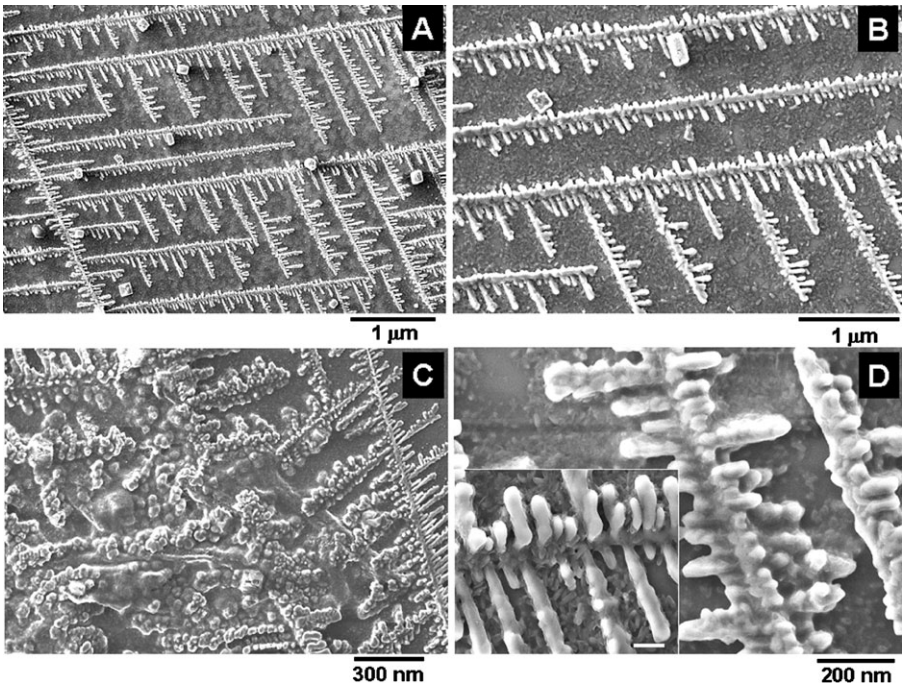

Fig. 6 (A–D) SEM images of $CaCO_3$ crystals at different magnifications, grown in the Hele–Shaw cell with an organic phase viscosity of 0.046 Pa s. The inset in D shows a magnified view of the main image with a scale bar of 100 nm.

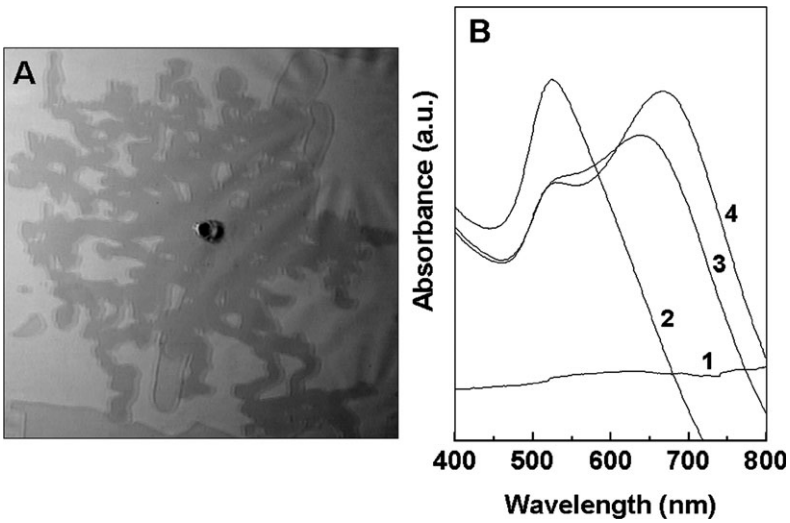

Fig. 7 (A) Image of the viscous-finger pattern formed after injection of an aqueous solution of borohydride reduced gold nanoparticles (colored phase) into the ethylenediamine–toluene–paraffin solution ($\eta = 0.046$ Pa s; transparent phase). (B) UV-vis spectra recorded from: curve 1—pure paraffin solution; curve 2—borohydride reduced aqueous gold nanoparticle solution; curve 3—gold nanoparticles assembled in the Hele–Shaw cell during the injection of an aqueous solution of borohydride reduced gold nanoparticles into the diamine–toluene–paraffin mixture ($\eta = 0.046$ Pa s); curve 4—gold nanoparticles assembled in the Hele–Shaw cell during the injection of chloroform containing diamine into borohydride reduced aqueous gold nanoparticles.

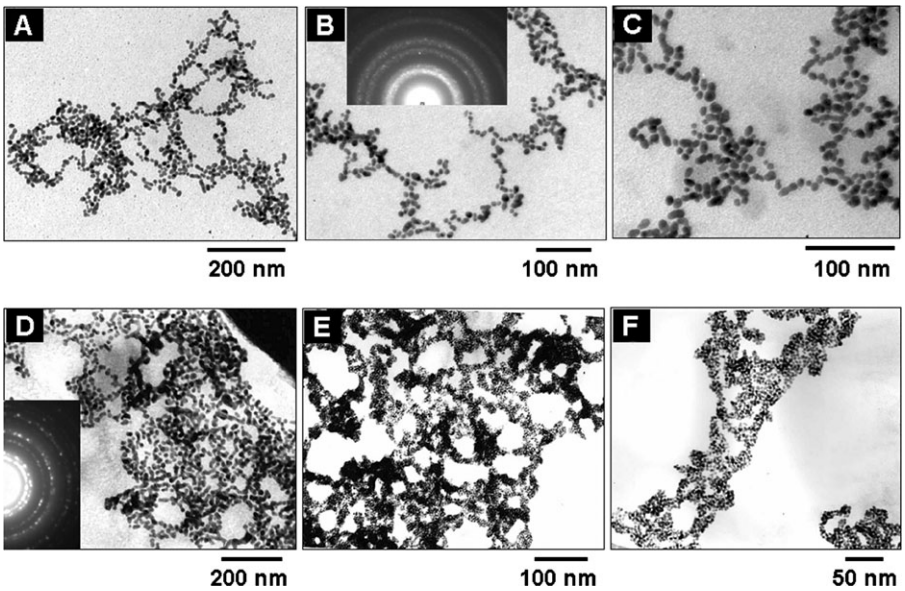

Fig. 8 (A–C) TEM images at different magnifications of gold nanoparticles assembled in the Hele–Shaw cell during the injection of an aqueous solution of borohydride reduced gold nanoparticles into the ethylenediamine–toluene–paraffin solution ($\eta = 0.046$ Pa s). (D–F) TEM images at different magnifications of gold nanoparticles grown in the Hele–Shaw cell during the injection of chloroform containing diamine into borohydride reduced aqueous gold nanoparticles. The insets in B and D show the SAED patterns recorded from the gold nanoparticles formed in both the experiments.

from the UV-vis measurements, the gold nanoparticles are assembled into quasi-linear superstructures (Fig. 8A and B). The selected area electron diffraction (SAED) analysis of the nanoparticles shown in Fig. 8B yielded a sharp diffraction pattern characteristic of fcc gold (inset, Fig. 8B). The highly open, quasi-linear structure of the gold nanoparticle assemblies is very clearly seen in Fig. 8C. The fact that the particles do not aggregate into dense structures normally observed during destabilization of nanoparticles in solution indicates that the crosslinking agent coupled with the assembly at the interface is responsible for the superstructures observed in the Hele–Shaw cell.

In order to understand the role of the solution viscosity and whether the nature of the solvent has any role to play in the nanoparticle assembly, an experiment was performed wherein chloroform containing diamine was injected into an aqueous solution of borohydride reduced gold nanoparticles (taken as the viscous fluid) without any attempts at increasing the viscosity by the addition of paraffin. The UV-vis spectrum recorded from the gold nanoparticle solution collected from this experiment is shown as curve 4 in Fig. 7B. Two absorption bands at 520 and 668 nm are observed in the UV-vis spectrum. The main difference with respect to the previous experiment is the shift in the in-plane plasmon vibration to a longer wavelength of 668 nm indicating the formation of more extended open nanoparticle assemblies. Fig. 8D–F show TEM images recorded at different magnification of Au nanoparticle assemblies observed in the Hele–Shaw cell experiment during the displacement of aqueous solution of gold nanoparticles by the diamine–chloroform solution. Dense networks of Au nanoparticles are observed in the TEM images (Fig. 8D and E) and in terms of extent and complexity of packing differ greatly from that observed in the earlier experiment. The magnified TEM image (Fig. 8F) reveals that the Au nanoparticle networks consist of smaller clusters of well separated Au nanoparticles. The formation of clusters of nanoparticles and their subsequent assembly into networks may be responsible for the shift towards longer wavelengths (668 nm) in the UV-vis spectrum from this sample (curve 4 in Fig. 7B).

In conclusion, we have shown that a dynamic liquid–liquid interface is a highly versatile medium for growing and assembling minerals as well as in the assembly of metal nanoparticles. The viscosity of the organic phase and thereby the nature of the viscous fingering interfacial structures obtained could be varied leading to differences in the morphology of the calcite crystals grown at the

interface. These effects also influence the assembly of gold nanoparticles *via* bifunctional cross-linkers at the interface. These results demonstrate the versatility of the expanding liquid–liquid interface in a Hele–Shaw cell in designing new materials and suggests great potential for development. It also brings up a number of fundamental issues related to the interface and how they may influence the inorganic structures formed. While the complexity of the interface does play an important role, it is not yet clear how hydrodynamic flows at the interface affect the reaction rate of ions at the interface (calcium and carbonate ions in this study) or how they influence the superstructure of gold nanoparticle assemblies. Rational design of the interface together with a better understanding of hydrodynamic flow issues and diffusion time scales of reacting species need to be developed in order to add value to this method for materials design and synthesis.

Acknowledgements

D. R. thanks the Department of Science and Technology (DST), Government of India for a research fellowship. We acknowledge the SEM/EDAX, TEM and XRD facilities of the Center for Materials Characterization, NCL Pune.

References

1 S. Mann and G. A. Ozin, *Nature (London)*, 1996, **382**, 313.
2 E. Matijevic, *Curr. Opin. Colloid Interface Sci.*, 1996, **1**, 176.
3 B. R. Heywood and S. Mann, *Langmuir*, 1992, **8**, 1492.
4 B. R. Heywood and S. Mann, *J. Am. Chem. Soc.*, 1992, **114**, 4681.
5 A. L. Litvin, S. Valiyaveettil, D. L. Kaplan and S. Mann, *Adv. Mater.*, 1997, **9**, 124.
6 D. Rautaray, S. R. Sainkar, N. R. Pawaskar and M. Sastry, *CrystEngComm.*, 2002, **4**, 626.
7 M. Sastry, K. S. Mayya, V. Patil, D. V. Paranjape and S. G. Hegde, *J. Phys. Chem. B*, 1997, **101**, 4954.
8 V. Patil, K. S. Mayya, S. D. Pradhan and M. Sastry, *J. Am. Chem. Soc.*, 1997, **119**, 9281.
9 M. Sastry, K. S. Mayya and V. Patil, *Langmuir*, 1998, **14**, 5921.
10 D. Rautaray, A. Kumar, S. Reddy, S. R. Sainkar, N. R. Pawaskar and M. Sastry, *CrystEngComm*, 2001, 45.
11 K. S. Mayya and M. Sastry, *Langmuir*, 1999, **15**, 1902.
12 J. Kuther, G. Nelles, R. Seshadri, M. Schaub, H. J. Butt and W. Tremel, *Chem. Eur. J.*, 1998, **4**, 1834.
13 J. Aizenberg, A. J. Black and G. M. Whitesides, *J. Am. Chem. Soc.*, 1999, **121**, 4500.
14 V. L. Colvin, A. N. Goldstein and A. P. Alivisatos, *J. Am. Chem. Soc.*, 1992, **114**, 522.
15 K. Bandyopadhyay, V. Patil, K. Vijayamohanan and M. Sastry, *Langmuir*, 1997, **13**, 5244.
16 D. Rautaray, A. Kumar, S. Reddy, S. R. Sainkar and M. Sastry, *Cryst. Growth Des.*, 2002, **2**, 197.
17 C. Damle, A. Kumar, M. Bhagwat, S. R. Sainkar and M. Sastry, *Langmuir*, 2002, **18**, 6075.
18 S. Mandal, S. Phadtare, P. R. Selvakannan, R. Pasricha and M. Sastry, *Nanotechnology*, 2003, **14**, 878.
19 S. Feng and T. Bein, *Science (Washington, D. C.)*, 1994, **265**, 1839.
20 G. Falini, M. Gazzano and A. Ripamonti, *Adv. Mater.*, 1994, **6**, 46.
21 J. J. J. M. Donners, R. J. M. Nolte and N. A. J. M. Sommerdijk, *J. Am. Chem. Soc.*, 2002, **124**, 9700.
22 T. Takahashi, H. Yui and T. Sawada, *J. Phys. Chem. B*, 2002, **106**, 2314.
23 J. J. Krueger, M. D. Amiridis and H. J. Ploehn, *Ind. Eng. Chem. Res.*, 2001, **40**, 3158.
24 Y. Selzer and D. Mandler, *J. Phys. Chem. B*, 2000, **104**, 4903.
25 L. X. Dang, *J. Phys. Chem. B*, 1999, **103**, 39.
26 Y. Uchiyama, I. Tsuyumoto, T. Kitamori and T. Sawada, *J. Phys. Chem. B*, 1999, **103**, 4663.
27 G. D. Yadav and C. A. Reddy, *Ind. Eng. Chem. Res.*, 1999, **38**, 2245.
28 H. S. Wu, *Chem. Eng. Sci.*, 1996, **51**, 827.
29 A. Bhattacharya, *Ind. Eng. Chem. Res.*, 1996, **35**, 645.
30 Y. Chen, Z. Gao, F. Li, L. Ge, M. Zhang, D. Zhan and Y. Shao, *Anal. Chem.*, 2003, **75**, 6593.
31 C. M. Starks, *J. Am. Chem. Soc.*, 1971, **93**, 195.
32 Z. Zhang, I. Tsuyumoto, S. Takahashi, T. Kitamori and T. Sawada, *J. Phys. Chem. A*, 1997, **101**, 4163.
33 Z. Zhang, I. Tsuyumoto, S. Takahashi, T. Kitamori and T. Sawada, *J. Phys. Chem. B*, 1998, **102**, 10 284.
34 P. Pieranski, *Phys. Rev. Lett.*, 1980, **45**, 569.
35 O. D. Velev, K. Furusawa and K. Nagayama, *Langmuir*, 1996, **12**, 2374.
36 Y. Lin, H. Skaff, T. Emrick, A. D. Dinsmore and T. P. Russell, *Science (Washington, D. C.)*, 2003, **299**, 226.
37 D. Yogev and S. Efrima, *J. Phys. Chem.*, 1988, **92**, 5754.
38 H. Schwartz, Y. Harel and S. Efrima, *Langmuir*, 2001, **17**, 3884.
39 K. S. Mayya and M. Sastry, *Langmuir*, 1999, **15**, 1902.
40 D. Wyrwa, N. Beyer and G. Schmid, *Nano Lett.*, 2002, **2**, 419.
41 A. D. Dinsmore, M. F. Hsu, M. G. Nikolaides, M. Marquez, A. R. Bausch and D. A. Weitz, *Science (Washington, D. C.)*, 2002, **298**, 1006.

42 Y. Lin, H. Skaff, A. Boker, A. D. Dinsmore, T. Emrick and T. P. Russell, *J. Am. Chem. Soc.*, 2003, **125**, 12 690.
43 M. G. Nikolaides, A. R. Bausch, M. F. Hsu, A. D. Dinsmore, M. P. Brenner and D. A. Weitz, *Nature (London)*, 2002, **420**, 299.
44 H. Jensen, D. J. Fermyn, J. E. Moser and H. H. Girault, *J. Phys. Chem. B*, 2002, **106**, 10 908.
45 D. J. Fermyn, H. Jensen, J. E. Moser and H. H. Girault, *Chem. Phys. Chem.*, 2003, **4**, 85.
46 T. Shioya, S. Nishizawa and N. Teramae, *J. Am. Chem. Soc.*, 1998, **120**, 11 534.
47 P. Liljeroth, A. Malkia, V. J. Cunnane, A. K. Kontturi and K. Kontturi, *Langmuir*, 2000, **16**, 6667.
48 E. Squitieri and I. Benjamin, *J. Phys. Chem. B*, 2001, **105**, 6412.
49 C. Fradin, D. Luzet, A. Braslau, M. Alba, F. Muller and J. Daillant, *Langmuir*, 1998, **14**, 26.
50 A. Gajraj and R. Y. Ofoli, *Langmuir*, 2000, **16**, 4279.
51 E. Dickinson, S. R. Euston and C. M. Woskett, *Prog. Colloid Polym. Sci.*, 1990, **82**, 65.
52 K. M. McGrath, *Adv. Mater.*, 2001, **13**, 989.
53 B. R. Heywood and S. Mann, *Adv. Mater.*, 1994, **6**, 9.
54 D. Walsh and S. Mann, *Adv. Mater.*, 1997, **9**, 658.
55 L. Qi, J. Li and J. Ma, *Adv. Mater.*, 2002, **14**, 300.
56 I. Lee, S. W. Han, H. J. Choi and K. Kim, *Adv. Mater.*, 2001, **13**, 1617.
57 J. Kunther, R. Seshadri, G. Nelles, H. J. Butt, W. Knoll and W. Tremel, *Adv. Mater.*, 1998, **10**, 401.
58 J. Kuther, R. Seshadri, G. Nelles, W. Assenmacher, H. J. Butt, W. Mader and W. Tremel, *Chem. Mater.*, 1999, **11**, 1317.
59 R. P. Andres, T. Bein, M. Dorogi, S. Feng, J. J. Henderson, C. P. Kubiak, W. Mahoney, R. G. Osifchin and R. Reifenberger, *Science (Washington, D. C.)*, 1996, **272**, 1323.
60 P. Galletto, P. F. Brevet, H. H. Girault, R. Antoine and M. Broyer, *J. Phys. Chem. B*, 1999, **103**, 8706.
61 C. P. Collier, R. J. Saykally, J. J. Shiang, S. E. Henriches and J. R. Heath, *Science (Washington, D. C.)*, 1997, **277**, 1978.
62 Z. L. Wang, *Adv. Mater.*, 1998, **10**, 13.
63 F. G. Freeman, K. C. Grabar, K. J. Allison, R. M. Bright, G. A. Davis, A. P. Guthrrie, M. B. Hommer, M. A. Jackson, P. C. Smith, D. G. Walter and M. J. Natan, *Science (Washington, D. C.)*, 1995, **267**, 1629.
64 M. Giersig and P. Mulvaney, *J. Phys. Chem.*, 1993, **97**, 6334.
65 J. Y. Lao, J. Y. Huang, D. Z. Wang, J. G. Wen and Z. F. Ren, *Nano Lett.*, 2003, **3**, 235.
66 S. Sharma and M. K. Sunkara, *J. Am. Chem. Soc.*, 2002, **124**, 12 288.
67 M. Li, H. Schnablegger and S. Mann, *Nature (London)*, 1999, **402**, 393.
68 J. D. Hopwood and S. Mann, *Chem. Mater.*, 1997, **9**, 1819.
69 M. Li and S. Mann, *Langmuir*, 2000, **16**, 7088.
70 M. Summers, J. Eastoe and S. Davis, *Langmuir*, 2002, **18**, 5023.
71 The radial Hele–Shaw cell is a simple set-up to study the phenomenon of viscous fingering and the factors that control the finger patterns. Such 'fingers' are formed during displacement of a viscous fluid by a less viscous one and this phenomenon has important implications in secondary oil recovery, electrochemical deposition, combustion and fluid flow in porous media. E. Ben-Jacob and P. Garik, *Nature (London)*, 1990, **343**, 523 and references therein. While the Hele–Shaw cell has been used extensively in understanding the underlying physics of dynamic instabilities at liquid–liquid interfaces, its use in chemistry in probing surfactant-mediated interfacial recognition events has only recently been attempted M. Sastry, A. Gole, A. G. Banpurkar, A. V. Limaye and S. B. Ogale, *Curr. Sci.*, 2001, **81**, 191. We are not aware of any report on the synthesis of materials in a Hele–Shaw cell.
72 D. Rautaray, A. Banpurkar, S. R. Sainkar, A. V. Limaye, S. Ogale and M. Sastry, *Cryst. Growth Des.*, 2003, **3**, 449.
73 D. Rautaray, A. Banpurkar, S. R. Sainkar, A. V. Limaye, N. R. Pavaskar, S. Ogale and M. Sastry, *Adv. Mater.*, 2003, **15**, 1273.
74 D. Bonn, H. Kellay, B. M. Amar and J. Meunier, *Phys. Rev. Lett.*, 1995, **75**, 2132.
75 G. Falini, S. Albeck, S. Weiner and L. Addadi, *Science (Washington, D. C.)*, 1996, **271**, 67.
76 *Spectrometric Identification of Organic Compounds*, ed. R. M. Silverstein and F. X. Webster, John Wiley and Sons, Inc., New York, 6th edn., p. 107.
77 The XRD patterns were indexed with reference to the unit cell of the calcite structure ($a = b = 4.989$ Å, $c = 17.062$ Å, space group D^6_{3D}-$R3c$, ASTM, chart card no. 5-0586) from ASTM chart.
78 C. A. Orme, A. Noy, A. Wierzbicki, M. T. McBride, M. Grantham, H. H. Teng, P. M. Dove and J. J. DeYoreo, *Nature (London)*, 2001, **411**, 775.
79 A. Sugawara, T. Ishii and T. Kato, *Angew. Chem., Int. Ed. Engl.*, 2003, **42**, 5299.
80 A. Kumar, S. Mandal, P. R. Selvakannan, R. Pasricha, A. B. Mandale and M. Sastry, *Langmuir*, 2003, **19**, 6277.
81 L. O. Brown and J. E. Hutchison, *J. Am. Chem. Soc.*, 1999, **121**, 882.
82 L. O. Brown and J. E. Hutchison, *J. Phys. Chem. B*, 2001, **105**, 8911.
83 D. V. Leff, L. Brandt and J. R. Heath, *Langmuir*, 1996, **12**, 4723.
84 M. Green and P. O'Brien, *Chem. Commun.*, 2000, 183.
85 T. Jensen, L. Lelly, A. Lazarides and G. C. Schatz, *J. Cluster. Sci.*, 1999, **10**, 295.